Accepted to Phys. Fluids 10.1063/5.0191550

Scaling laws for natural convection boundary layer of a $Pr > 1$ fluid on a vertical solid surface subject to a sinusoidal temperature in a linearly-stratified ambient fluid

Wenxian Lin (林文宪),[1, a)] S. W. Armfield,[2] and Mehdi Khatamifar[1]

[1)] *College of Science & Engineering, James Cook University, Townsville, QLD 4811, Australia*

[2)] *School of Aerospace, Mechanical and Mechatronic Engineering, The University of Sydney, NSW 2006, Australia*

(Dated: 30 December 2023)

The understanding of the transient behavior of natural convection boundary layer (NCBL) on a heated vertical solid surface under various heating conditions is of fundamental significance and application importance. In this study, scalings for the parameters representing the behavior of unsteady NCBL flow of a linearly-stratified $Pr > 1$ fluid on a semi-infinite vertical solid surface heated with a time-varying sinusoidal temperature at different development stages are developed with a scaling analysis, in terms of Ra, Pr, s and f_n, which are the Rayleigh number, Prandtl number, stratification number and frequency of the sinusoidal temperature, respectively. These scalings are validated and quantified with a series of numerical simulations over wide ranges of Ra, Pr, s, and f_n. The frequency of the fluctuations experienced by the NCBL behavior at the transitional stage, due to the stratification of the ambient fluid, is also analysed, and it is shown that the previously obtained scaling for the unsteady NCBL case with the constant heat flux heating condition is basically applicable for the current case, Ra and f_n have additional effects as well due to the time-varying nature of the applied temperature.

[a)] Electronic mail: wenxian.lin@jcu.edu.au.

Accepted to Phys. Fluids 10.1063/5.0191550

I. INTRODUCTION

As a classic fluid mechanical and heat transfer problem, the natural convection boundary-layer (abbreviated as 'NCBL' hereafter) flow under various heating conditions and different configurations is of fundamental significance and practical application importance, making it a topic which has drawn enormous research and is still heavily studied (see *e.g.*,[1–12]). Among that under numerous heating conditions and configurations, the unsteady NCBL on a heated vertical solid surface (abbreviated as 'VSS' hereafter) with time-varying heating conditions, particularly that in a sinusoidal temperature or heat flux, is the main mechanism for numerous practical applications, such as for many solar thermal technologies like in a Trombe wall in a solar house[13–15], in a solar air collector[16,17], in a solar chimney[18–20], etc. Although there are many studies on this specific topic[2,3,5–7,11,12,21–41], our current understanding of the transient behavior of such NCBL on VSS heated with time-varying conditions in stratified ambient fluids is still very limited.

We have studied the unsteady NCBL on VSS heating by both constant and time-varying temperature and heat flux in both homogeneous and linearly-stratified ambient fluids with a wide range of Pr (see, *e.g.*, [11,21,22,24,26,27,42–47]). We obtained, through scaling analysis, the scalings for the key parameters which characterize the behavior of unsteady NCBL flow, which include the wall temperature, thermal boundary-layer (abbreviated as 'TBL' hereafter) thickness, viscous boundary-layer (abbreviated as 'VBL' hereafter) thickness, maximum vertical velocity within the VBL, the Nusselt number, and the corresponding time scales typifying the various flow development stages. These scalings predict quantitatively these parameters in terms of the control parameters of NCBL flow, *i.e.*, the Rayleigh number (Ra), Prandtl number (Pr), frequency of the time-varying heating flux or temperature, and stratification parameter of the ambient fluid. They were validated by numerical results obtained over large ranges of the control parameters.

In the present study, we extended our previous studies to the case in which the unsteady NCBL flow is on a VSS subject to a sinusoidal temperature in a linearly-stratified ambient fluid with $Pr > 1$. We achieve the aim by conducting a similar scaling analysis to develop the corresponding scalings for the characteristic parameters of the behavior of the unsteady NCBL flow, which are then validated and quantified with a series of numerical simulations over wide ranges of the control parameters.

Accepted to Phys. Fluids 10.1063/5.0191550

II. PHYSICAL AND COMPUTATIONAL MODELS

A. Physical model

The physical model considered here is a VSS of length H, which is without thickness and placed in a Pr $>$ 1 Newtonian fluid that is linearly-stratified, and is heated by a sinusoidal temperature (ST), as sketched in Fig. 1. It is assumed that the unsteady NCBL flow formed along the VSS is laminar and two-dimensional. The stratified ambient fluid is initially stationary and at the constant temperature gradient $S_a = dT_{a,0}(Y)/dY$ in the vertical direction (Y-direction), where $T_{a,0}(Y)$ is the initial temperature of the ambient fluid at height Y (at time $t = 0$) and S_a is the ambient stratification parameter. Along the VSS ($0 \leq Y \leq H$), the temperature imposed on it, $T_w(t)$, changes sinusoidally with time as follows,

$$T_w(t) = T_{w,m}\sin(2\pi ft) + T_{a,0}(H), \tag{1}$$

in which $T_{w,m}$ is the magnitude of the ST, which is also the characteristic temperature (*i.e.*, temperature scale), f is the frequency of the ST, and $T_{a,0}(H)$ is the initial temperature of the ambient fluid at height H, which is the height where the VSS ends at the top. The origin is at $X = 0$ and $Y = 0$, where X is the horizontal coordinate. It is assumed that X and Y are positive in the right and upward directions, respectively.

At time t, the local temperature inside the fluid at Y is $T(Y)$, so a local fluctuating temperature, $T_f(Y)$, away from the initial ambient temperature at Y, can be defined as follows,

$$T_f(Y) = T(Y) - T_{a,0}(Y). \tag{2}$$

This means that the local fluctuating temperature imposed on the VSS at the height Y (*i.e.*, the VSS temperature in terms of fluctuating temperature) is,

$$T_{w,f}(t) = T_w(t) - T_{a,0}(Y) = T_{w,m}\sin(2\pi ft) + T_{a,0}(H) - T_{a,0}(Y). \tag{3}$$

As $T_{a,0}(H) = T_{a,0}(Y = 0) + S_aH$ and $T_{a,0}(Y) = T_{a,0}(Y = 0) + S_aY$, Eq. (3) becomes,

$$T_{w,f}(t) = T_{w,m}\sin(2\pi ft) + S_a(H - Y). \tag{4}$$

It should be noted that, in terms of the fluctuating temperature, the fluctuating temperature imposed on the VSS, $T_{w,f}(t)$, is not constant along the VSS (*i.e.*, it changes with

Accepted to Phys. Fluids 10.1063/5.0191550

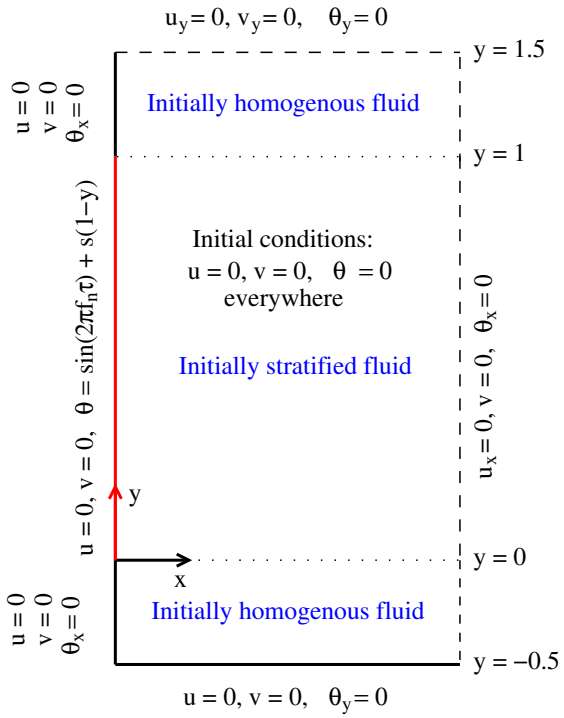

FIG. 1. Sketch of the physical model, computational domain and initial and boundary conditions.

Y). If $T_{w,f}(t)$ is constant along the VSS, the physical model considered will not be the time-varying 'temperature' case, but the time-varying 'heat flux' case instead.

B. Computational model

The governing equations for the unsteady NCBL flow, with the Boussinesq approximation for buoyancy, are written as follows in terms of $T_f(Y)$ (but for brevity, T_f is used),

$$\frac{\partial U}{\partial X} + \frac{\partial V}{\partial Y} = 0, \tag{5}$$

$$\frac{\partial U}{\partial t} + U\frac{\partial U}{\partial X} + V\frac{\partial U}{\partial Y} = -\frac{1}{\rho}\frac{\partial P}{\partial X} + \nu\left(\frac{\partial^2 U}{\partial X^2} + \frac{\partial^2 U}{\partial Y^2}\right), \tag{6}$$

$$\frac{\partial V}{\partial t} + U\frac{\partial V}{\partial X} + V\frac{\partial V}{\partial Y} = -\frac{1}{\rho}\frac{\partial P}{\partial Y} + \nu\left(\frac{\partial^2 V}{\partial X^2} + \frac{\partial^2 V}{\partial Y^2}\right) + g\beta T_f, \tag{7}$$

$$\frac{\partial T_f}{\partial t} + U\frac{\partial T_f}{\partial X} + V\frac{\partial T_f}{\partial Y} + VS_a = \kappa\left(\frac{\partial^2 T_f}{\partial X^2} + \frac{\partial^2 T_f}{\partial Y^2}\right). \tag{8}$$

where U and V are the velocity components in the X and Y directions, P is pressure, ρ, β, κ and ν are the density, coefficient of thermal expansion, thermal diffusivity and kinematic viscosity of fluid, respectively, and g is the gravitational acceleration which is in the negative Y direction.

The parameters in the above governing equations can be made dimensionless by using the following relations.

$$x = \frac{X}{H}, \quad y = \frac{Y}{H}, \quad u = \frac{U}{V_0}, \quad v = \frac{V}{V_0}, \quad \tau = \frac{t}{(H/V_0)},$$

$$p = \frac{P}{\rho V_0^2}, \quad \theta_f = \frac{T_f}{T_{w,m}},$$

in which $V_0 = \kappa Ra^{1/2}/H$ is the velocity scale and Ra is the Rayleigh number which is defined as,

$$Ra = \frac{g\beta T_{w,m} H^3}{\nu\kappa}. \tag{9}$$

In addition to Ra, the Prandtl number Pr, the dimensionless frequency of the sinusoidal temperaturef_n, and the dimensionless stratification number s are other control parameters for the unsteady NCBL flow considered. These parameters are defined as follows,

$$Pr = \frac{\nu}{\kappa}, \tag{10}$$

$$s = \frac{d\theta_{a,0}(y)}{dy} = \frac{d[T_{a,0}(Y)/T_{w,m}]}{d(Y/H)} = \frac{H}{T_{w,m}}\frac{d[T_{a,0}(Y)]}{d(Y)} = \frac{H}{T_{w,m}}S_a, \tag{11}$$

$$f_n = \frac{f}{V_0/H} = \frac{0.5/t_{ht}}{V_0/H} = \frac{0.5}{\tau_{ht}}, \tag{12}$$

where t_{ht} is the total heating time duration of the sinusoidal temperature and $\tau_{ht} = t_{ht}/(H/V_0)$ is its dimensionless form. In accordance with the clear sky solar radiation model[13], only the heating part is considered in the present study, thus $2\pi f t_{ht} = \pi$, so $f = 0.5/t_{ht}$ which leads to $f_n = 0.5/\tau_{ht}$. Nevertheless, the scaling laws developed in the present study are widely applicable for many other situations in addition to the unsteady NCBL cases caused by the sinusoidal solar radiation.

The above governing equations (5)-(8) can then be written in the dimensionless forms as follows,

$$\frac{\partial u}{\partial x} + \frac{\partial v}{\partial y} = 0, \tag{13}$$

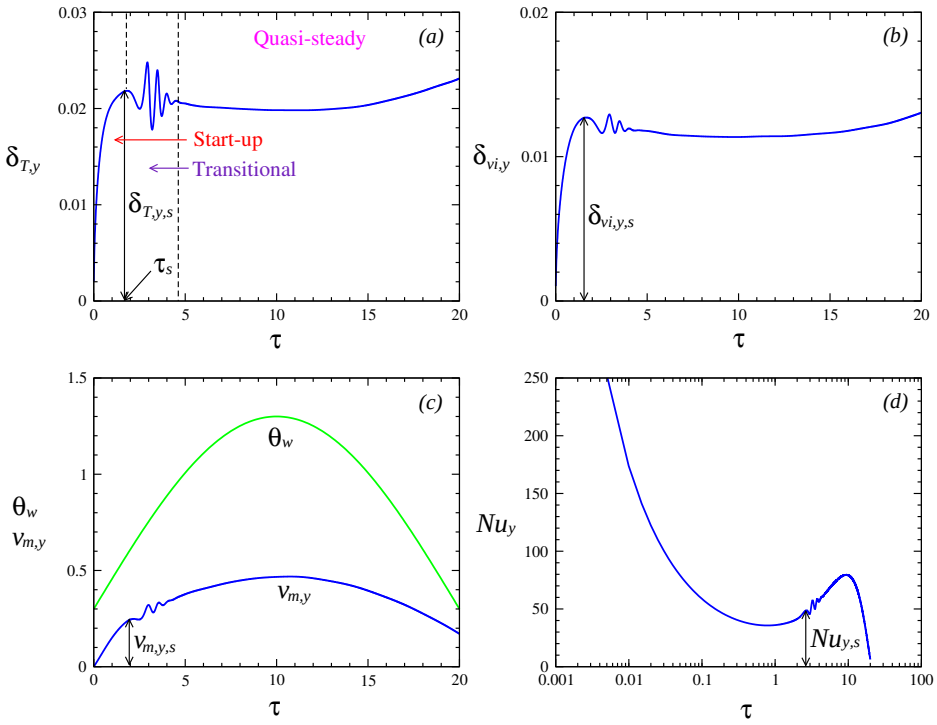

FIG. 2. Time series of $\delta_{T,y}$, $\delta_{vi,y}$, $v_{m,y}$, and Nu_y at $y = 0.7$ for the DNS case with $Pr = 10$, $Ra = 10^8$, $s = 1$ and $f_n = 0.025$ (DNS Case 3).

$$\frac{\partial u}{\partial \tau} + u\frac{\partial u}{\partial x} + v\frac{\partial u}{\partial y} = -\frac{\partial p}{\partial x} + \frac{Pr}{Ra^{1/2}}\left(\frac{\partial^2 u}{\partial x^2} + \frac{\partial^2 u}{\partial y^2}\right), \tag{14}$$

$$\frac{\partial v}{\partial \tau} + u\frac{\partial v}{\partial x} + v\frac{\partial v}{\partial y} = -\frac{\partial p}{\partial y} + \frac{Pr}{Ra^{1/2}}\left(\frac{\partial^2 v}{\partial x^2} + \frac{\partial^2 v}{\partial y^2}\right) + Pr\theta_f, \tag{15}$$

$$\frac{\partial \theta_f}{\partial \tau} + u\frac{\partial \theta_f}{\partial x} + v\frac{\partial \theta_f}{\partial y} + vs = \frac{1}{Ra^{1/2}}\left(\frac{\partial^2 \theta_f}{\partial s^2} + \frac{\partial^2 \theta_f}{\partial y^2}\right). \tag{16}$$

III. SCALING ANALYSIS

For the cases considered in this paper, there are four major dimensionless parameters to characterize the BL behavior at the dimensionless height y, *i.e.*, the dimensionless TBL thickness, $\delta_{T,y}$, the dimensionless inner VBL thickness, $\delta_{vi,y}$, the dimensionless maximum

vertical velocity within the VBL, $v_{m,y}$ which occurs at $x = \delta_{vi,y}$, and the Nusselt number on the VSS, Nu_y. $\delta_{T,y}$ and $\delta_{vi,y}$ are made dimensionless by H, while $v_{m,y}$ is made dimensionless by V_0. Nu_y is determined by

$$Nu_y = \left[\frac{\partial \theta_f(y)}{\partial x}\right]_{x=0}. \tag{17}$$

Figure 2 depicts, as a representation, the numerically obtained time series of these four parameters at $y = 0.7$ for the case with $Pr = 10$, $Ra = 10^8$, $s = 1$ and $f_n = 0.025$ (DNS Case 3 as listed in Table I). From this figure, it is seen that the development of both $\delta_{T,y}$ and $\delta_{vi,y}$ experience three distinct stages; the start-up stage (abbreviated as 'SUS' hereafter), which is in general small, in which $\delta_{T,y}$ and $\delta_{vi,y}$ increase monotonically and quickly; this is followed by the transitional stage, in which $\delta_{T,y}$ and $\delta_{vi,y}$ fluctuate at a frequency mainly related to s due to the stratification of the ambient fluid, as will be shown later; and eventually the quasi-steady stage (abbreviated as 'QSS' hereafter) which is generally much longer and in which both $\delta_{T,y}$ and $\delta_{vi,y}$ only have small variations. The development of $v_{m,y}$ is different; although $v_{m,y}$ has similar developments in the first two stages to that for $\delta_{T,y}$ and $\delta_{vi,y}$, it differs significantly in the QSS, as it basically follows the trend of θ_w, which is the dimensionless sinusoidal temperature imposed on the VSS, although they still have distinct differences, *e.g.*, at the end of the heating, $v_{m,y}$ does not become zero, but is at a finite value. The development of Nu_y is also different; it reduces substantially and very rapidly in the SUS, but becomes to increase in the transitional stage and the early part of the QSS, followed by the substantial reductions to approach essentially zero at the end of the heating, apparently as then no heat transfers from the VSS to the fluid anymore.

The scalings for these characteristic parameters at the SUP and QSS will be obtained in the subsequent scaling analysis whereas the scalings at the transitional stage cannot be developed. As the exact times for the end of the SUS and the transitional stage are not easily defined and thus not uniquely determined, to quantitatively validate the obtained scalings at the SUS and QSS with the DNS results, it will be appropriate to just assume that the BL development consists of the SUS and QSS only, with τ_s, which is the time when $\delta_{T,y}$ attains the maximum for the first time, as the time scale for both the end of the SUS and the commencement of the QSS, as τ_s is a unique time that can be determined numerically, as shown in Fig. 2. Although no scalings for these four parameters can not be developed at the transitional stage, the frequency of the fluctuations of these parameters in the transitional stage can be numerically obtained and will be compared to the available relevant scaling.

We follow the same procedure as taken by us in the past studies on the unsteady NCBL flows with different heating conditions and configurations, in particular that in[22,26,27,42,44–46]. Some details in the following scaling analysis are therefore not repeated as they can be found in these past studies.

A. At the SUS

As shown in Lin *et al.*[42], by balancing the unsteady and diffusion terms in Eq. (16) over the TBL at height y gives,

$$\delta_{T,y} \sim \frac{\tau^{1/2}}{Ra^{1/4}}. \tag{18}$$

For $Pr > 1$ fluid, the inner VBL thickness at height y, according to Lin *et al.*[22], has the following relation with $\delta_{T,y}$,

$$\delta_{vi,y} \sim \frac{1}{(1+Pr^{-1/2})}\delta_{T,y} \sim \frac{\tau^{1/2}}{(1+Pr^{-1/2})Ra^{1/4}}, \tag{19}$$

and the buoyancy force is balanced by the viscous force in Eq. (15), which leads to the following transient vertical velocity scale at height y at time τ[22,27],

$$v_{m,y} \sim \frac{Ra^{1/2}\Delta\theta_{f,y}\delta_{T,y}^2}{(1+Pr^{-1/2})^2} \sim \frac{\Delta\theta_{f,y}\tau}{(1+Pr^{-1/2})^2} \sim \frac{[\sin(2\pi f_n\tau)+s(1-y)]\tau}{(1+Pr^{-1/2})^2} \tag{20}$$

where

$$\Delta\theta_{f,y} = \theta_{w,f} = \frac{T_{w,f}(t)}{T_{w,m}} = \frac{T_{w,m}\sin(2\pi ft) + S_a(H-Y)}{T_{w,m}} = \sin(2\pi f_n\tau) + s(1-y). \tag{21}$$

It should be noted that $\Delta\theta_{f,y} = \theta_{w,f} - \theta_{a,f} = \theta_{w,f}$ as $\theta_{a,f}$ is zero because the fluctuating temperature of the ambient fluid is zero. The local Nusselt number at the SUS is then as follows,

$$Nu_y = \left[\frac{\partial\theta_f(y)}{\partial x}\right]_{x=0} \sim \frac{\Delta\theta_{f,y}}{\delta_{T,y}} \sim \frac{[\sin(2\pi f_n\tau)+s(1-y)]Ra^{1/4}}{\tau^{1/2}}. \tag{22}$$

Eqs. (18), (19), (20), and (22) are therefore the scalings for $\delta_{T,y}$, $\delta_{vi,y}$, $v_{m,y}$, and Nu_y at the SUS.

B. At the QSS

The growth of the boundary layer continues, with heat convected vertically by the velocity represented by Eq. (20), until the heat conducted in from the boundary balances

that convected away, and subsequently the boundary layer attains the QSS. Hence, from Eq. (16), the balance becomes,

$$v_{m,y}\left(\frac{\Delta\theta_{f,y}}{y}+s\right)\sim\frac{1}{Ra^{1/2}}\frac{\Delta\theta_{f,y}}{\delta_{T,y}^2}. \tag{23}$$

Putting Eq. (20) for $v_{m,y}$ and Eq. (18) for $\delta_{T,y}$ into Eq. (23) yields,

$$\frac{\Delta\theta_{f,y}\tau}{(1+Pr^{-1/2})^2}\left(\frac{\Delta\theta_{f,y}}{y}+s\right)\sim\frac{\Delta\theta_{f,y}}{\tau}, \tag{24}$$

which gives,

$$\tau_s\sim\frac{(1+Pr^{-1/2})}{\left(\frac{\Delta\theta_{f,y}}{y}+s\right)^{1/2}}\sim\frac{(1+Pr^{-1/2})y^{1/2}}{[\sin(2\pi f_n\tau_s)+s]^{1/2}}. \tag{25}$$

This is the time scale for the boundary layer growth to reach the QSS.

At this time scale, the scalings for $\delta_{T,y,s}$, $\delta_{vi,y,s}$, $v_{m,y,s}$, and $Nu_{y,s}$, which are the respective scales for $\delta_{T,y}$, $\delta_{vi,y}$, $v_{m,y}$, and Nu_y at the QSS, respectively, can be obtained as follows: putting Eq. (25) into Eq. (18) gives,

$$\delta_{T,y,s}\sim\frac{\tau_s^{1/2}}{Ra^{1/4}}\sim\frac{(1+Pr^{-1/2})^{1/2}y^{1/4}}{[\sin(2\pi f_n\tau_s)+s]^{1/4}Ra^{1/4}}; \tag{26}$$

putting Eq. (25) into Eq. (19) gives,

$$\delta_{vi,y,s}\sim\frac{1}{(1+Pr^{-1/2})}\delta_{T,y,s}\sim\frac{y^{1/4}}{(1+Pr^{-1/2})^{1/2}[\sin(2\pi f_n\tau_s)+s]^{1/4}Ra^{1/4}}; \tag{27}$$

putting Eq. (25) into Eq. (20) gives,

$$\begin{aligned}v_{m,y,s}&\sim\frac{[\sin(2\pi f_n\tau_s)+s(1-y)]\tau_s}{(1+Pr^{-1/2})^2}\\&\sim\frac{[\sin(2\pi f_n\tau_s)+s(1-y)]\tau_s}{(1+Pr^{-1/2})^2}\frac{(1+Pr^{-1/2})y^{1/2}}{[\sin(2\pi f_n\tau_s)+s]^{1/2}}\\&\sim\frac{[\sin(2\pi f_n\tau_s)+s(1-y)]y^{1/2}}{(1+Pr^{-1/2})[\sin(2\pi f_n\tau_s)+s]^{1/2}};\end{aligned} \tag{28}$$

and putting Eq. (25) into Eq. (22) gives,

$$Nu_{y,s}\sim\frac{[\sin(2\pi f_n\tau_s)+s(1-y)][\sin(2\pi f_n\tau_s)+s]^{1/4}Ra^{1/4}}{(1+Pr^{-1/2})^{1/2}y^{1/4}}. \tag{29}$$

It is worth noting that if the ambient fluid is not stratified, *i.e.*, $s=0$, the above scalings will become exactly the same for the unstratified case, as obtained by Lin & Armfield[27], which are as follows:

At the SUS:

$$\delta_{T,y} \sim \frac{\tau^{1/2}}{Ra^{1/4}}. \tag{30}$$

$$\delta_{vi,y} \sim \frac{\tau^{1/2}}{(1+Pr^{-1/2})Ra^{1/4}}, \tag{31}$$

$$v_{m,y} \sim \frac{\sin(2\pi f_n \tau)\tau}{(1+Pr^{-1/2})^2}, \tag{32}$$

$$Nu_y \sim \frac{[\sin(2\pi f_n \tau)]Ra^{1/4}}{\tau^{1/2}}. \tag{33}$$

At the QSS:

$$\tau_s \sim \frac{(1+Pr^{-1/2})y^{1/2}}{[\sin(2\pi f_n \tau_s)]^{1/2}}. \tag{34}$$

$$\delta_{T,y,s} \sim \frac{(1+Pr^{-1/2})^{1/2}y^{1/4}}{[\sin(2\pi f_n \tau_s)]^{1/4}Ra^{1/4}}; \tag{35}$$

$$\delta_{vi,y,s} \sim \frac{y^{1/4}}{(1+Pr^{-1/2})^{1/2}[\sin(2\pi f_n \tau_s)]^{1/4}Ra^{1/4}}; \tag{36}$$

$$v_{m,y,s} \sim \frac{[\sin(2\pi f_n \tau_s)]^{1/2}y^{1/2}}{(1+Pr^{-1/2})}; \tag{37}$$

$$Nu_{y,s} \sim \frac{[\sin(2\pi f_n \tau_s)]^{5/4}Ra^{1/4}}{(1+Pr^{-1/2})^{1/2}y^{1/4}}. \tag{38}$$

It should be emphasized that all the above scaling relations are obtained and hence valid under the assumption that τ_{ht} is larger than τ_s.

IV. NUMERICAL VALIDATION OF THE SCALINGS

A. DNS runs

In the present study, all numerical simulations were conducted in a dimensionless 1×2 computational domain with a mesh of 599×599 nodes, as sketched in Fig. 1. The use of the extra regions with the dimensionless height of 0.5 above and below the plate is to minimize the effect of the boundaries, as commonly used for such problems (see, *e.g.*,[11,21,22,24,26,27,43–48]). The initial and boundary conditions used are listed below:

$$u = v = 0,\ \theta = 0 \text{ at all } x,\ y \text{ when } \tau < 0;$$

and

$$u = v = 0,\ \theta_x = 0 \text{ at } x = 0,\ -0.5 \le y \le 0;$$

$$u = v = 0,\ \theta = \sin(2\pi f_n \tau) + s(1-y) \text{ at } x = 0,\ 0 \le y \le 1;$$

$$u = v = 0,\ \theta_x = 0 \text{ at } x = 0,\ 1 \le y \le 1.5;$$

$$u_x = v = \theta_x = 0 \text{ at } x = 1,\ -0.5 \le y \le 1.5;$$

$$u = v = 0,\ \theta_y = 0 \text{ at } 0 \le x \le 1,\ y = -0.5;$$

$$u_y = v_y = \theta_y = 0 \text{ at } 0 \le x \le 1,\ y = 1.5 \text{ when } \tau \ge 0,$$

where the subscripts 'x' and 'y' denote the partial derivatives of a parameter with respect to x and y, respectively.

The scalings obtained above are assessed and validated numerically with numerical simulations. To examine the roles of Ra, Pr, s and f_n in the scalings, a total of 16 DNS runs were carried out, with details of these runs presented in Table I; four runs (Runs 1-5) are at varying Ra over $10^6 \le Ra \le 10^9$ with fixed $Pr = 10$, $s = 1$ and $f_n = 0.025$ to show the Ra dependence; five runs (Runs 3, 9-12) are at varying Pr over $5 \le Pr \le 100$ with fixed $Ra = 10^8$, $s = 1$ and $f_n = 0.025$ to show the Pr dependence; five runs (Runs 3, 5-8) are for the variation of s in the range of $0.2 \le s \le 5$ at $Ra = 10^8$, Pr = 10 and $f_n = 0.025$ to show the s dependence; and five runs (Runs 3 and 13-16) are for the variation of f_n over $0.005 \le f_n \le 0.1$ at fixed $Ra = 10^8$, $s = 1$ and Pr = 10 to illustrate the f_n dependence. As the scaling laws are developed assuming $Pr \gg 1$, the minimum value of Pr selected is 5.

All numerical simulations were conducted with our in-house code used in[26,45,46] and a series of our other past studies, such as[24,44,48]. As the numerical methodology, meshes, benchmarking of the code, etc., were detailed in those papers, particularly in[26,45], they will not be presented here to avoid repetition.

B. Validation of the scalings for the TBL thickness

The scaling for $\delta_{T,y}$ at the SUS is Eq. (18), which shows that only Ra has effect. This is apparently validated by the numerical results presented in the left column in Fig. 3, as only the time series of $\delta_{T,y}$ at different Ra values (DNS runs 1-4), as shown in Fig. 3(b), differ from each other, while the time series of $\delta_{T,y}$ at different y, s, Pr and f_n values are essentially the same when $Ra = 10^8$, as shown in Fig. 3(a), (c)-(e).

The scaling for $\delta_{T,y,s}$ at the QSS is Eq. (26), which indicates that all four control parameters (Ra, Pr, s and f_n) have effects on $\delta_{T,y,s}$ and $\delta_{T,y,s}$ varies at different height (y) as well.

Accepted to Phys. Fluids 10.1063/5.0191550

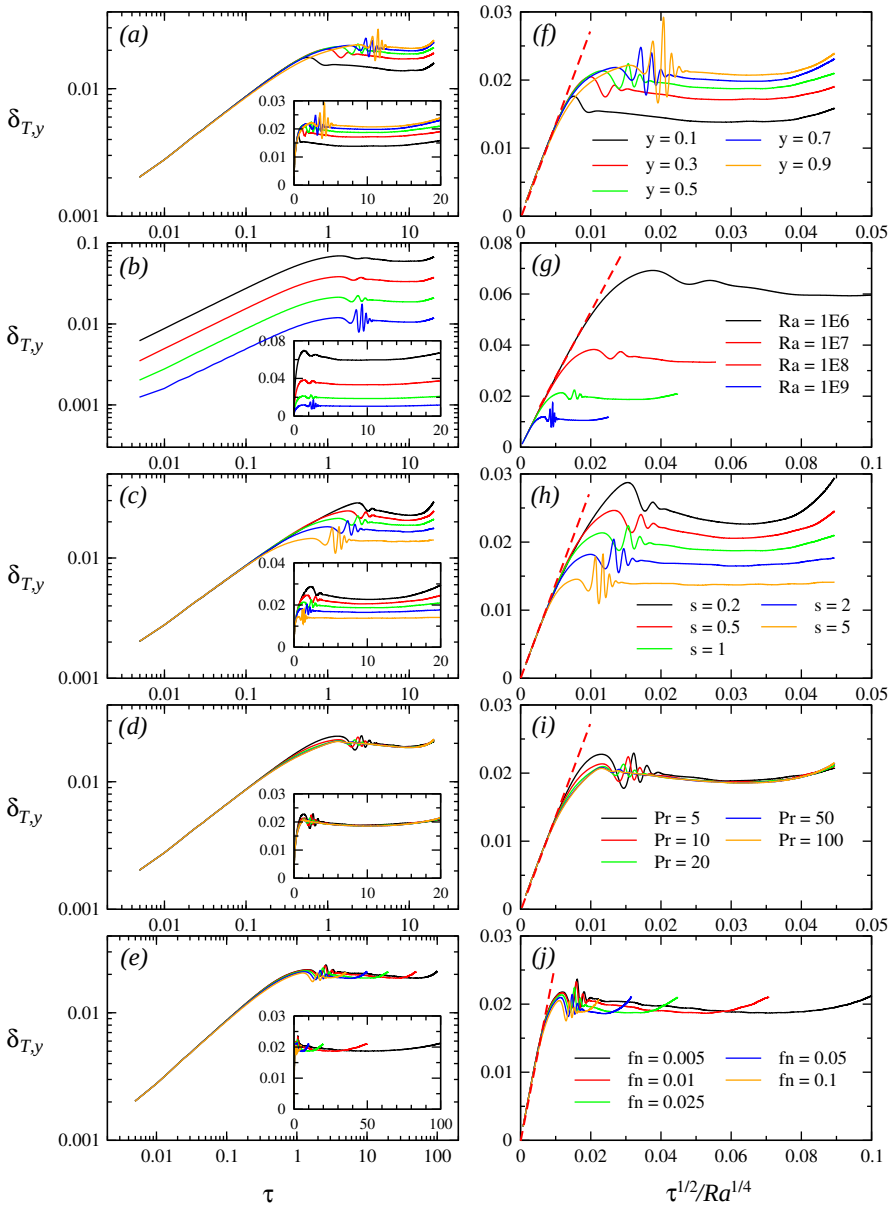

FIG. 3. Time series of $\delta_{T,y}$: raw data (left column) and scaled data (right column): (a) and (f) Run 3 with varying y; (b) and (g) Runs 1-4 with varying Ra at $y = 0.5$; (c) and (h) Runs 3, 5-8 with varying s at $y = 0.5$; (d) and (i) Runs 3, 9-12 with varying Pr at $y = 0.5$; and (e) and (j) Runs 3, 13-16 with varying f_n at $y = 0.5$.

TABLE I. Values of Ra, Pr, s, f_n, and τ_{ht} for the 16 numerical simulation runs.

Run	Ra	s	Pr	f_n	τ_{ht}
1	10^6	1	10	0.025	20
2	10^7	1	10	0.025	20
3	10^8	1	10	0.025	20
4	10^9	1	10	0.025	20
5	10^8	0.2	10	0.025	20
6	10^8	0.5	10	0.025	20
7	10^8	2	10	0.025	20
8	10^8	5	10	0.025	20
9	10^8	1	5	0.025	20
10	10^8	1	20	0.025	20
11	10^8	1	50	0.025	20
12	10^8	1	100	0.025	20
13	10^8	1	10	0.005	100
14	10^8	1	10	0.01	50
15	10^8	1	10	0.05	10
16	10^8	1	10	0.1	5

All these effects are clearly demonstrated by the numerical results presented in the right column in Fig. 3 as the time series of $\delta_{T,y,s}$ vary when any of the parameter changes.

To quantify the scaling (18) for $\delta_{T,y}$, the raw and scaled time series of all 16 DNS runs, each at a specific y value which is randomly selected, are presented in Fig. 4. From Fig. 4(b), it is seen that all scaled time series of $\delta_{T,y}$ plotted against $\tau^{1/2}/Ra^{1/4}$ within the SUS are essentially on the same line represented by

$$\delta_{T,y} = 2.741 \frac{\tau^{1/2}}{Ra^{1/4}}, \tag{39}$$

which confirms and quantified the scaling (18) for $\delta_{T,y}$.

With the definition of τ_s as shown in Fig. 2, the values of τ_s are obtained for all DNS runs, with each run at five heights (y = 0.1, 0.3, 0.5, 0.7, and 0.9) and the results are presented in Fig. 5. From Fig. 5(b), it is seen that the scaling (25) for τ_s, which is $\hat{\tau}_s$ =

Accepted to Phys. Fluids 10.1063/5.0191550

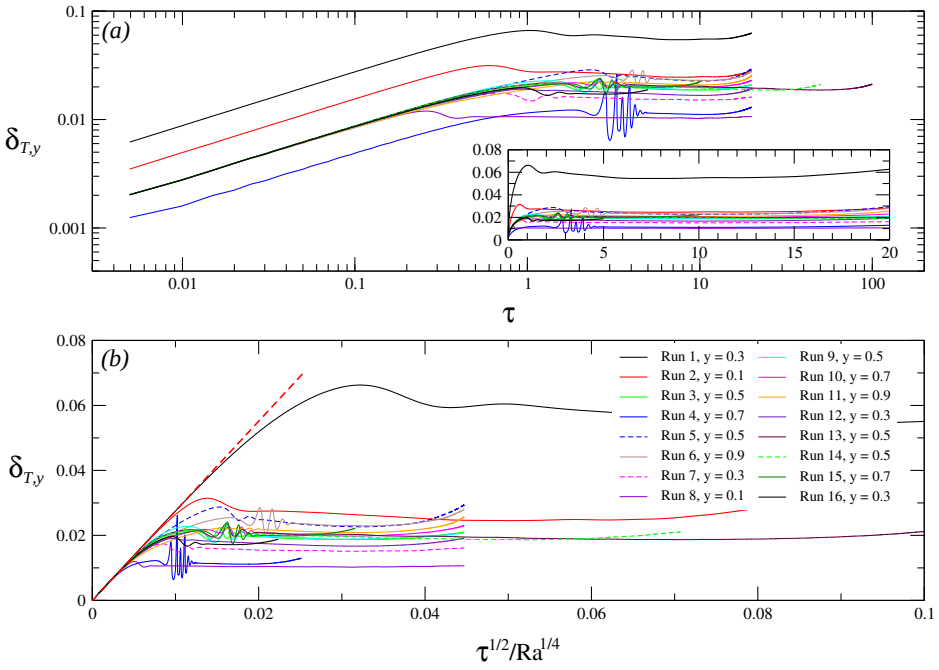

FIG. 4. (a) $\delta_{T,y}$ plotted against τ (raw data) and (b) $\delta_{T,y}$ plotted against $\tau^{1/2}/Ra^{1/4}$ (scaled data) for all 16 DNS runs, each at a specific y value. The red dashed line in (b) is the slope of $\delta_{T,y}$ plotted against $\tau^{1/2}/Ra^{1/4}$, which represents $\delta_{T,y} = 2.741\tau^{1/2}/Ra^{1/4}$.

$(1 + Pr^{-1/2})y^{1/2}/[\sin(2\pi f_n\tau_s) + s]^{1/2}$, collapses the numerically obtained τ_s approximately onto the following straight line, which is the linear fit obtained with the regression analysis with all data presented in Fig. 5(b),

$$\tau_s = 2.292\hat{\tau}_s - 0.344 = 2.292\frac{(1 + Pr^{-1/2})y^{1/2}}{[\sin(2\pi f_n\tau_s) + s]^{1/2}} - 0.344, \tag{40}$$

with the regression constant of $R = 0.9372$. The slope of 2.292 in the above equation represents the quantified empirical proportional constant between τ_s and $\hat{\tau}_s$. The noticeable deviations of the numerically obtained τ_s values away from the above linear fit are due to the some relatively large $\delta_{T,y,s}$ differences for different cases and at different heights, as shown in Figs. 3 and 4. Such noticeable deviations in τ_s result in large deviations in $\delta_{vi,y,s}$, $v_{m,y,s}$ and $Nu_{y,s}$, which are obtained at τ_s, as will be shown subsequently.

Accepted to Phys. Fluids 10.1063/5.0191550

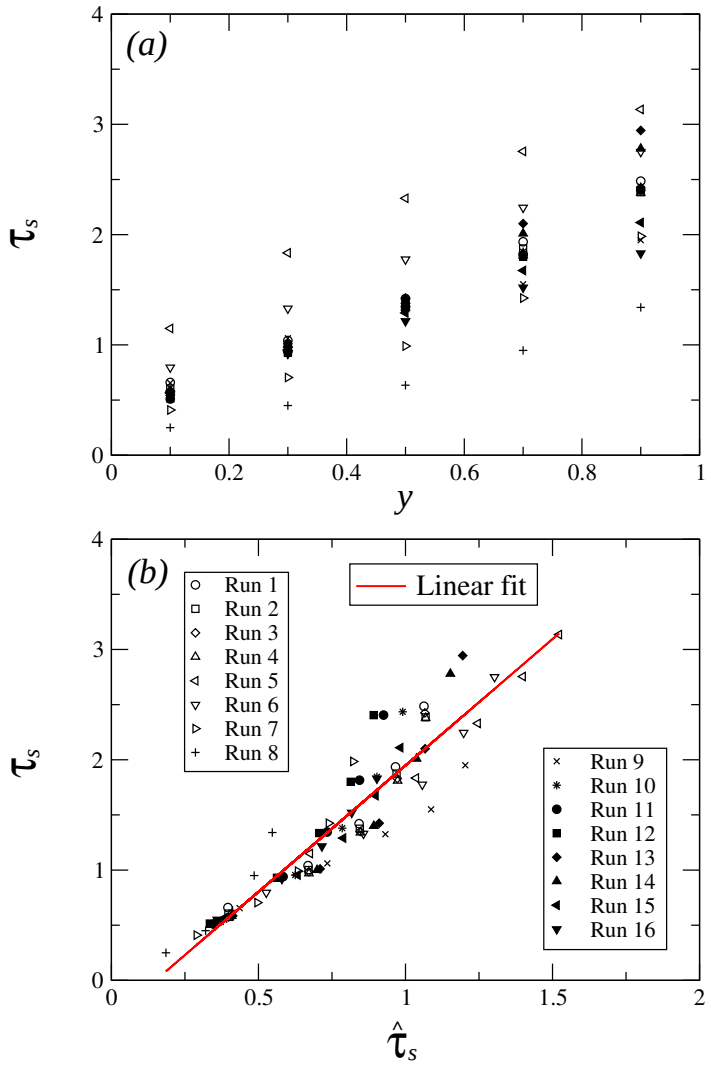

FIG. 5. (a) τ_s plotted against y (raw data) and (b) τ_s plotted against $\hat{\tau}_s$ (scaled data) for all 16 DNS runs, each at five y value ($y = 0.1$, 0.3, 0.5, 0.7, and 0.9). The red line in (b) represents the linear fit between τ_s and $\hat{\tau}_s$, where $\hat{\tau}_s = (1 + Pr^{-1/2})y^{1/2}/[\sin(2\pi f_n \tau_s) + s]^{1/2}$ is the scaling (25) for τ_s.

Accepted to Phys. Fluids 10.1063/5.0191550

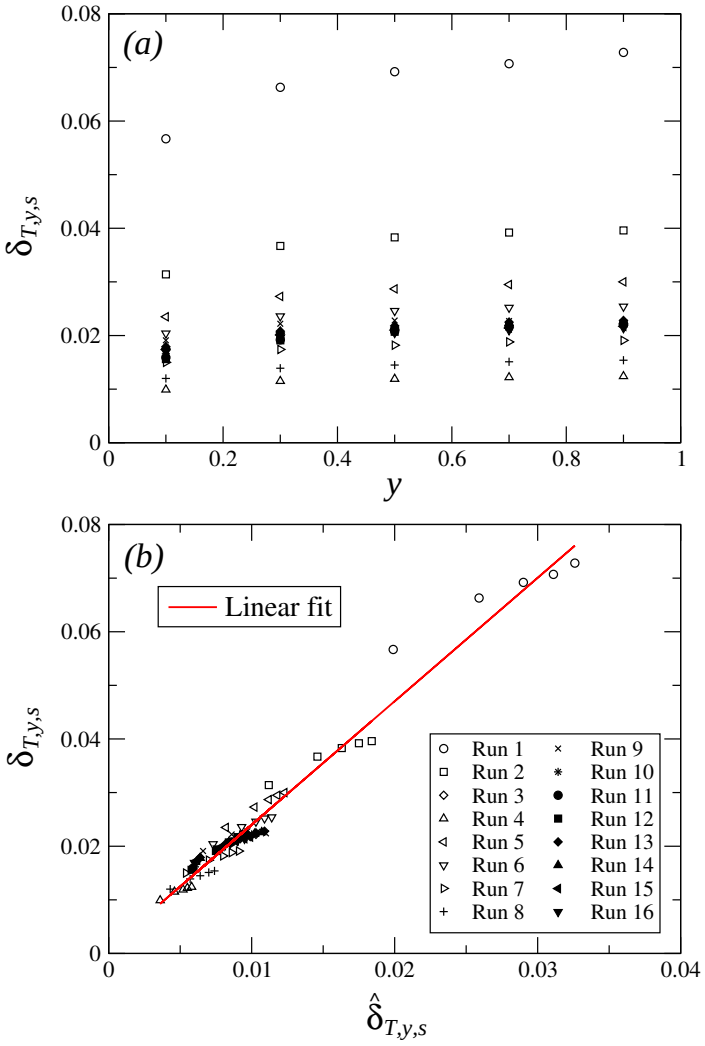

FIG. 6. (a) $\delta_{T,y,s}$ plotted against y (raw data) and (b) $\delta_{T,y,s}$ plotted against $\hat{\delta}_{T,y,s}$ (scaled data) for all 16 DNS runs, each at five y value ($y = 0.1$, 0.3, 0.5, 0.7, and 0.9). The red line in (b) represents the linear fit between $\delta_{T,y,s}$ and $\hat{\delta}_{T,y,s}$, where $\hat{\delta}_{T,y,s} = (1+Pr^{-1/2})^{1/2} y^{1/4}/[\sin(2\pi f_n \tau_s)+s]^{1/4}/Ra^{1/4}$ is the scaling (26) for $\delta_{T,y,s}$.

The scaling for $\delta_{T,y,s}$ at the QSS is Eq. (26). To see if this scaling can be validated by the numerical results, the numerically obtained $\delta_{T,y,s}$ values for all DNS runs, with each run at the five heights, are plotted in Fig. 6. From Fig. 6(b), it is seen that the scaling (26) for $\delta_{T,y,s}$, which is $\hat{\delta}_{T,y,s} = (1 + Pr^{-1/2})^{1/2} y^{1/4}/[\sin(2\pi f_n \tau_s) + s]^{1/4}/Ra^{1/4}$, collapses the numerically obtained $\delta_{T,y,s}$ approximately onto the following straight line, which is the linear fit obtained with the regression analysis with all data presented in Fig. 6(b),

$$\delta_{T,y,s} = 2.303\hat{\delta}_{T,y,s} + 0.001 = 2.303\frac{(1 + Pr^{-1/2})^{1/2} y^{1/4}}{[\sin(2\pi f_n \tau_s) + s]^{1/4} Ra^{1/4}} + 0.001, \tag{41}$$

with the regression constant of $R = 0.9845$. The slope of 2.303 in the above equation represents the quantified empirical proportional constant between $\delta_{T,y,s}$ and $\hat{\delta}_{T,y,s}$. The noticeable deviations of the numerically obtained $\delta_{T,y,s}$ values away from the above linear fit are due to the some relatively large $\delta_{T,y,s}$ differences for different cases and at different heights, as mentioned above.

The scalings for the other three parameters can be validated in the same way, as detailed below.

C. Validation of the scalings for the inner VBL thickness

The scaling for $\delta_{vi,y}$ at the SUS is Eq. (19), which shows that both Ra and Pr have effects. This is clearly validated by the numerical results presented in the left column in Fig. 7, as only the time series of $\delta_{vi,y}$ at different Ra values (DNS runs 1-4), as shown in Fig. 7(b), and that at different Pr, as shown in Fig. 7(d), differ from each other, while the time series of $\delta_{vi,y}$ at different y, s, and f_n values are essentially the same when $Ra = 10^8$ and $Pr = 10$, as shown in Fig. 7(a), (c), and (e).

The scaling for $\delta_{vi,y,s}$ at the QSS is Eq. (27), which indicates that all parameters Ra, Pr, s, f_n, and y have effects on $\delta_{vi,y,s}$. All these effects are clearly demonstrated by the numerical results presented in the right column in Fig. 7 as the time series of $\delta_{vi,y,s}$ vary when any of the parameters changes.

To quantify the scaling (19) for $\delta_{vi,y}$, the raw and scaled time series of all 16 DNS runs, each at a specific y value which is randomly selected, are presented in Fig. 8. From Fig. 8(b), it is seen that all scaled time series of $\delta_{vi,y}$ plotted against $\tau^{1/2}/(1 + Pr^{-1/2})/Ra^{1/4}$ within

Accepted to Phys. Fluids 10.1063/5.0191550

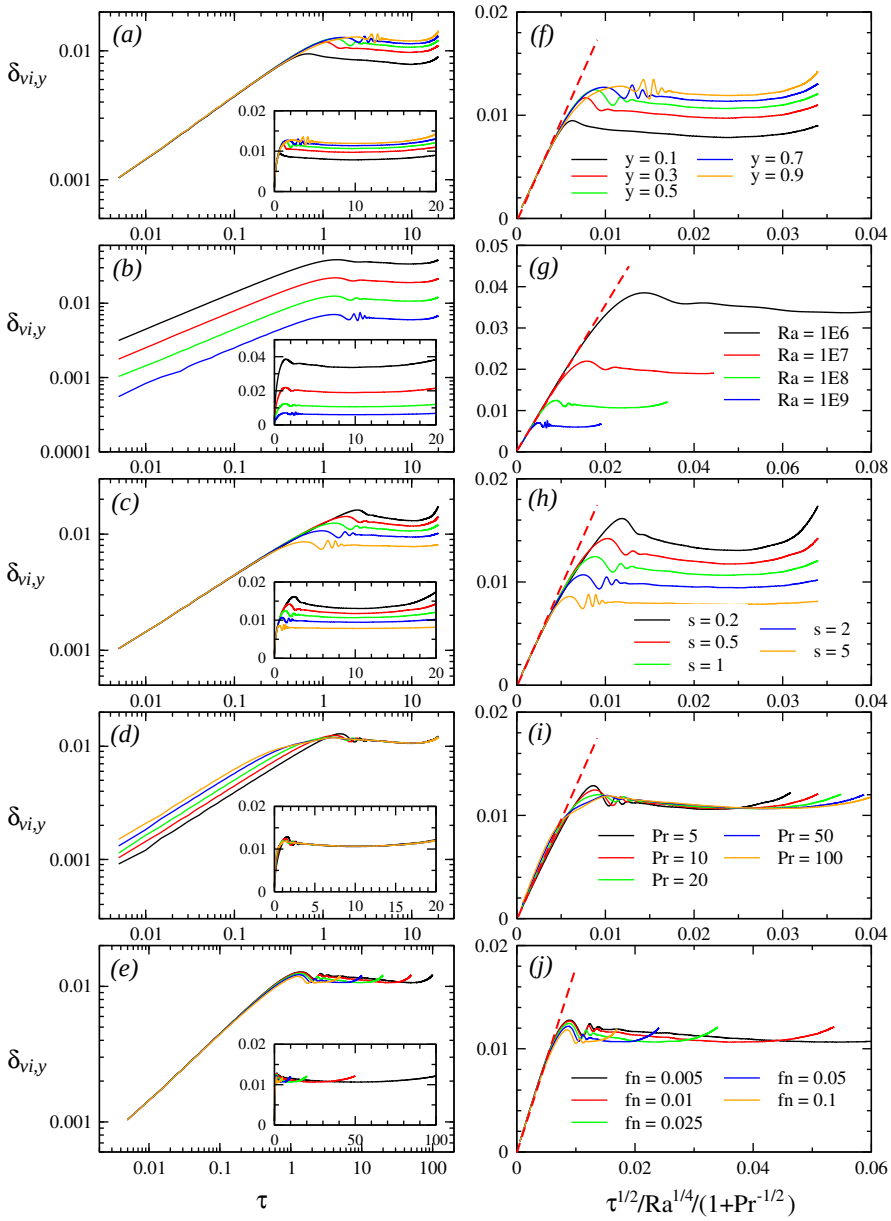

FIG. 7. Time series of $\delta_{vi,y}$: raw data (left column) and scaled data (right column): (a) and (f) Run 3 with varying y; (b) and (g) Runs 1-4 with varying Ra at $y = 0.5$; (c) and (h) Runs 3, 5-8 with varying s at $y = 0.5$; (d) and (i) Runs 3, 9-12 with varying Pr at $y = 0.5$; and (e) and (j) Runs 3, 13-16 with varying f_n at $y = 0.5$.

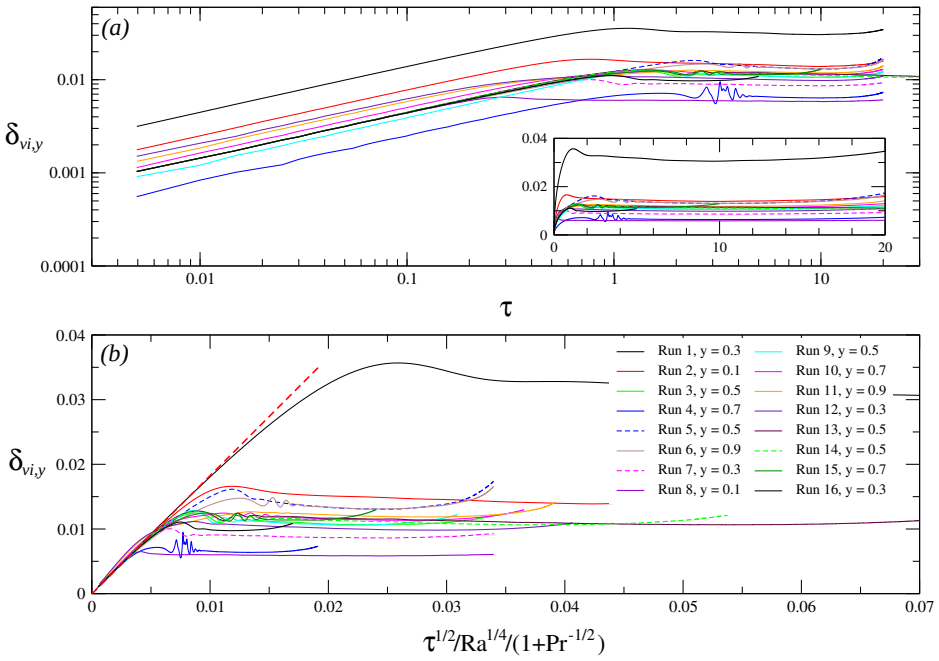

FIG. 8. (*a*) $\delta_{vi,y}$ plotted against τ (raw data) and (*b*) $\delta_{vi,y}$ plotted against $\tau^{1/2}/(1+Pr^{-1/2})/Ra^{1/4}$ (scaled data) for all 16 DNS runs, each at a specific y value. The red dashed line in (*b*) is the slope of $\delta_{vi,y}$ plotted against $\tau^{1/2}/(1+Pr^{-1/2})/Ra^{1/4}$, which represents $\delta_{vi,y} = 1.838\tau^{1/2}/(1+Pr^{-1/2})/Ra^{1/4}$.

the SUS are essentially on the same line represented by

$$\delta_{vi,y} = 1.838\frac{\tau^{1/2}}{(1+Pr^{-1/2})Ra^{1/4}}, \tag{42}$$

which confirms and quantified the scaling (19) for $\delta_{vi,y}$.

The scaling for $\delta_{vi,y,s}$ at the QSS is Eq. (27). To see if this scaling can be validated by the numerical results, the numerically obtained $\delta_{vi,y,s}$ values for all DNS runs, with each run at the five heights, are plotted in Fig. 9. From Fig. 9(*b*), it is seen that the scaling (27) for $\delta_{vi,y,s}$, which is $\hat{\delta}_{vi,y,s} = y^{1/4}/(1+Pr^{-1/2})^{1/2}/[sin(2\pi f_n\tau_s)+s]^{1/4}/Ra^{1/4}$, collapses the numerically obtained $\delta_{vi,y,s}$ approximately onto the following straight line, which is the

Accepted to Phys. Fluids 10.1063/5.0191550

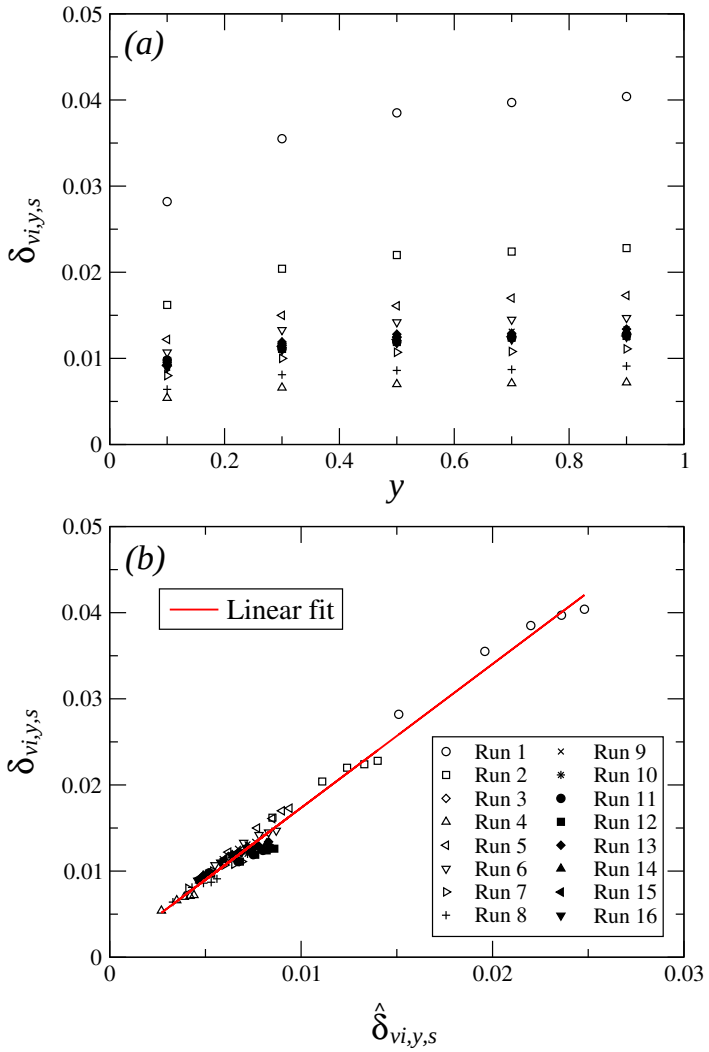

FIG. 9. (a) $\delta_{vi,y,s}$ plotted against y (raw data) and (b) $\delta_{vi,y,s}$ plotted against $\hat{\delta}_{vi,y,s}$ (scaled data) for all 16 DNS runs, each at five y value (y = 0.1, 0.3, 0.5, 0.7, and 0.9). The red line in (b) represents the linear fit between $\delta_{vi,y,s}$ and $\hat{\delta}_{vi,y,s}$, where $\hat{\delta}_{vi,y,s} = y^{1/4}/(1+Pr^{-1/2})^{1/2}/[\sin(2\pi f_n \tau_s)+s]^{1/4}/Ra^{1/4}$ is the scaling (27) for $\delta_{vi,y,s}$.

linear fit obtained with the regression analysis with all data presented in Fig. 9(b),

$$\begin{aligned}\delta_{vi,y,s} &= 1.669\hat{\delta}_{vi,y,s} + 0.00065 \\ &= 1.669\frac{y^{1/4}}{(1+Pr^{-1/2})^{1/2}[\sin(2\pi f_n\tau_s)+s]^{1/4}Ra^{1/4}} + 0.00065,\end{aligned} \tag{43}$$

with the regression constant of $R = 0.9904$. The slope of 1.669 in the above equation represents the quantified empirical proportional constant between $\delta_{vi,y,s}$ and $\hat{\delta}_{vi,y,s}$. The noticeable deviations of the numerically obtained $\delta_{vi,y,s}$ values away from the above linear fit are due to the same reason as mentioned above.

D. Validation of the scalings for the maximum vertical velocity

The scaling for $v_{m,y}$ at the SUS is Eq. (20), which shows that, with the exception of Ra, all other parameters (Pr, s, f_n and y) have effects. This is clearly validated by the numerical results presented in the left column in Fig. 10, as only the time series of $v_{m,y}$ at different Ra values (DNS runs 1-4), as shown in Fig. 10(b), do not vary at the SUS, while the time series of $v_{m,y}$ at other parameters differ from each other. It is noted that the effect of f_n on $v_{m,y}$ is mainly near the end of the SUS, as shown in Fig. 10(e).

The scaling for $v_{m,y,s}$ at the QSS is Eq. (28), which indicates that, again, with the exception of Ra, the other four parameters (Pr, s, f_n, and y) have effects on $v_{m,y,s}$. All these effects are clearly demonstrated by the numerical results presented in the right column in Fig. 10. It is worth noting that, although Ra has no effect on $v_{m,y,s}$ at the QSS, there are still differences of the fluctuations in the time series of $v_{m,y}$ at the QSS, as shown in Fig. 10(g).

To quantify the scaling (20) for $v_{m,y}$, the raw and scaled time series of all 16 DNS runs, each at a specific y value which is randomly selected, are presented in Fig. 11. From Fig. 11(b), it is seen that all scaled time series of $v_{m,y}$ plotted against $[\sin(2\pi f_n\tau)+s(1-y)]\tau/(1+Pr^{-1/2})^2$ within the SUS are essentially on the same line represented by

$$v_{m,y} = 0.816\frac{[\sin(2\pi f_n\tau)+s(1-y)]\tau}{(1+Pr^{-1/2})^2}, \tag{44}$$

which confirms and quantified the scaling (20) for $v_{m,y}$.

The scaling for $v_{m,y,s}$ at the QSS is Eq. (28). To see if this scaling can be validated by the numerical results, the numerically obtained $v_{m,y,s}$ values for all DNS runs, with each run at

Accepted to Phys. Fluids 10.1063/5.0191550

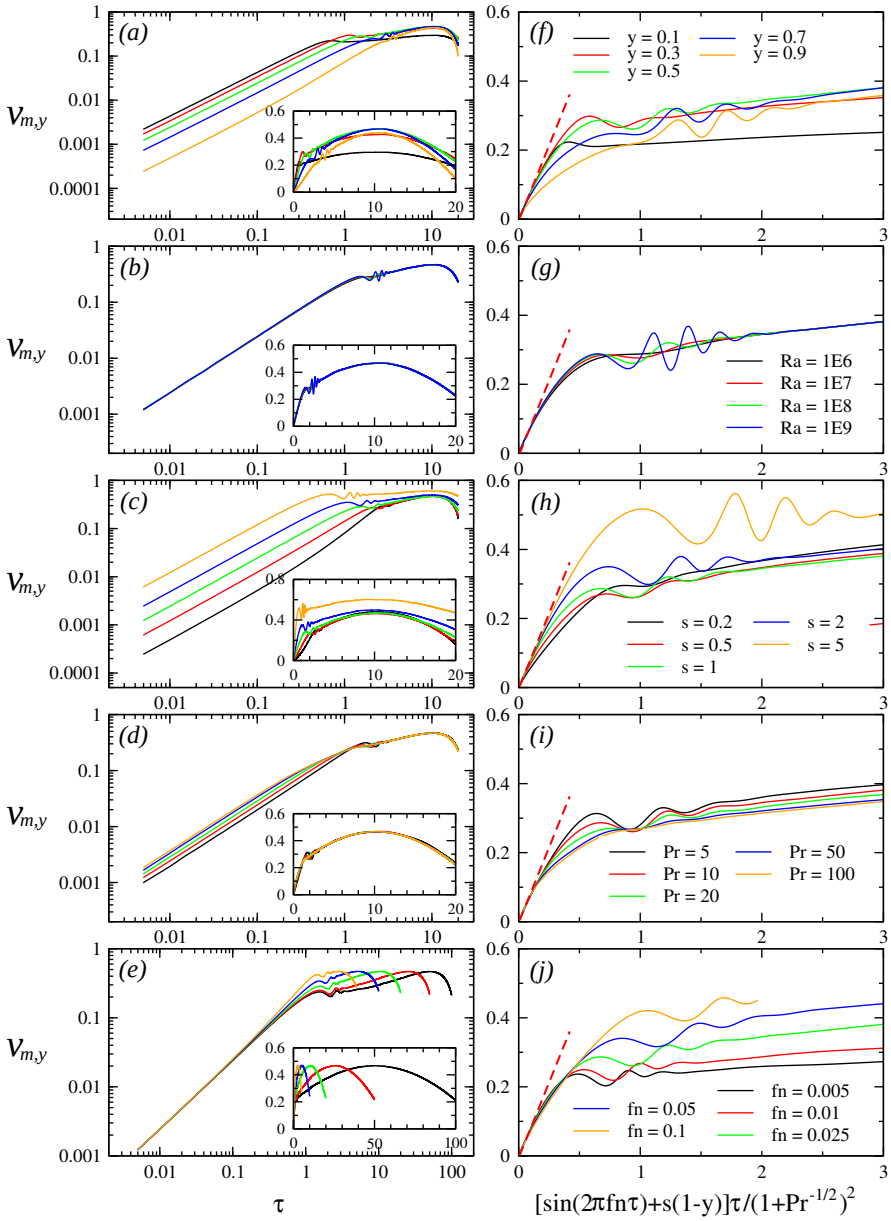

FIG. 10. Time series of $v_{m,y}$: raw data (left column) and scaled data (right column): (a) and (f) Run 3 with varying y; (b) and (g) Runs 1-4 with varying Ra at $y = 0.5$; (c) and (h) Runs 3, 5-8 with varying s at $y = 0.5$; (d) and (i) Runs 3, 9-12 with varying Pr at $y = 0.5$; and (e) and (j) Runs 3, 13-16 with varying f_n at $y = 0.5$.

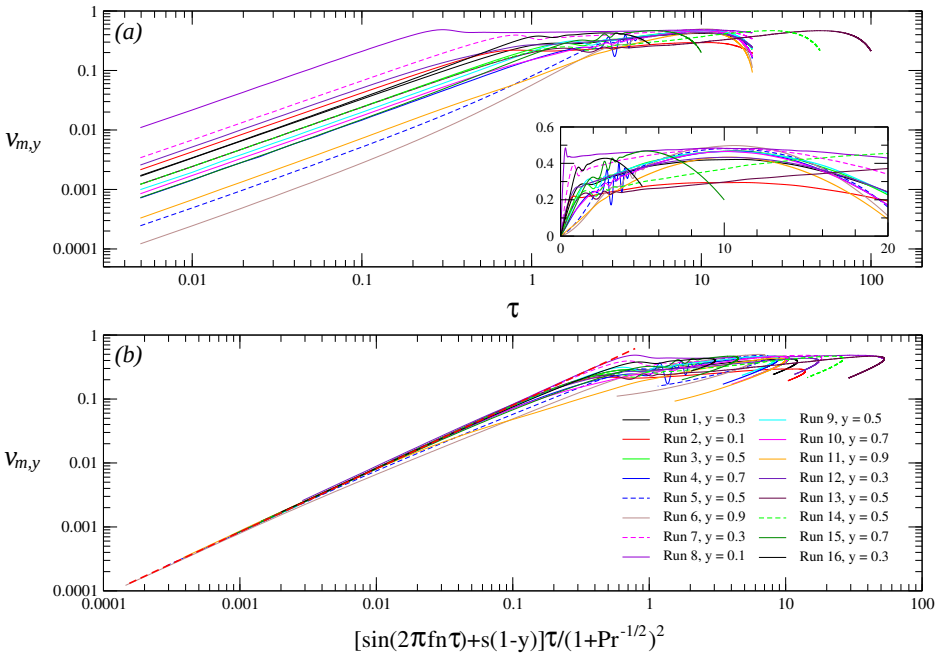

FIG. 11. (a) $v_{m,y}$ plotted against τ (raw data) and (b) $v_{m,y}$ plotted against $[\sin(2\pi f_n\tau) + s(1-y)]\tau/(1+Pr^{-1/2})^2$ (scaled data) for all 16 DNS runs, each at a specific y value. The red dashed line in (b) is the slope of $v_{m,y}$ plotted against $[\sin(2\pi f_n\tau) + s(1-y)]\tau/(1+Pr^{-1/2})^2$, which represents $v_{m,y} = 0.816[\sin(2\pi f_n\tau) + s(1-y)]\tau/(1+Pr^{-1/2})^2$.

the five heights, are plotted in Fig. 12. From Fig. 12(b), it is seen that the scaling (28) for $v_{m,y,s}$, which is $\hat{v}_{m,y,s} = [\sin(2\pi f_n\tau_s)+s(1-y)]y^{1/2}/[\sin(2\pi f_n\tau_s)+s]^{1/2}/(1+Pr^{-1/2})$, collapses the numerically obtained $v_{m,y,s}$ approximately onto the following straight line, which is the linear fit obtained with the regression analysis with all data presented in Fig. 12(b),

$$\begin{aligned} v_{m,y,s} &= 0.765\hat{v}_{m,y,s} + 0.003 \\ &= 0.765\frac{[\sin(2\pi f_n\tau_s) + s(1-y)]y^{1/2}}{[\sin(2\pi f_n\tau_s) + s]^{1/2}(1+Pr^{-1/2})} + 0.003, \end{aligned} \tag{45}$$

with the regression constant of $R = 0.9107$. Again the large deviations of the numerically obtained $v_{m,y,s}$ values away from the above linear fit are due to the same reason as mentioned above.

Accepted to Phys. Fluids 10.1063/5.0191550

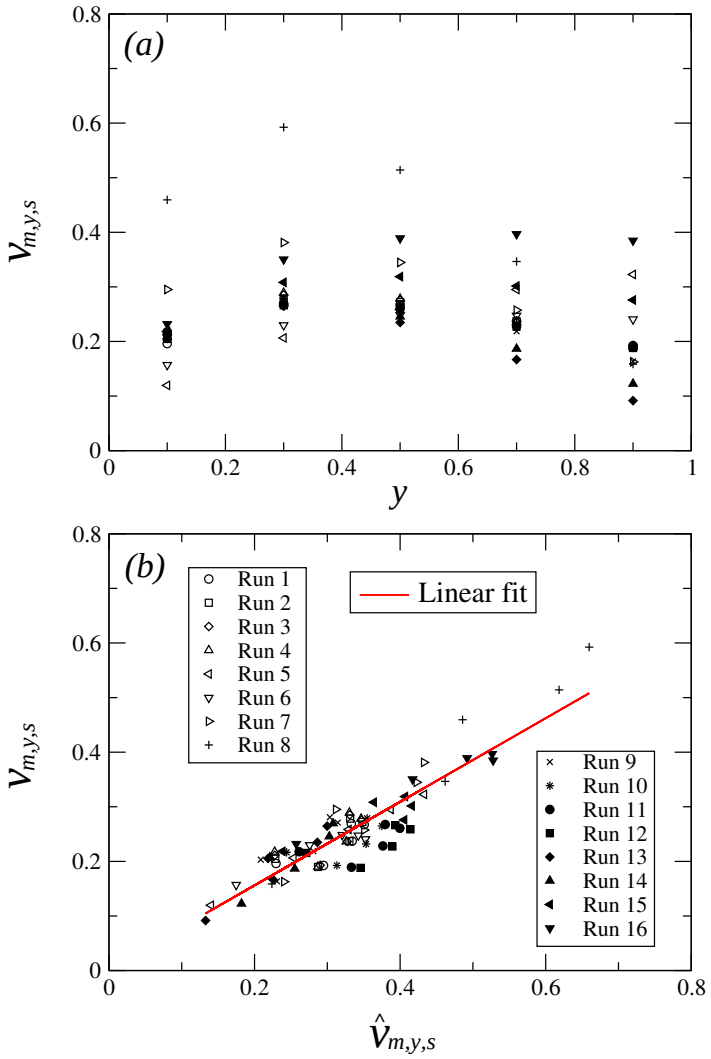

FIG. 12. (a) $v_{m,y,s}$ plotted against y (raw data) and (b) $v_{m,y,s}$ plotted against $\hat{v}_{m,y,s}$ (scaled data) for all 16 DNS runs, each at five y value ($y = 0.1$, 0.3, 0.5, 0.7, and 0.9). The red line in (b) represents the linear fit between $v_{m,y,s}$ and $\hat{v}_{m,y,s}$, where $\hat{v}_{m,y,s} = [\sin(2\pi f_n \tau_s) + s(1-y)]y^{1/2}/[\sin(2\pi f_n \tau_s) + s]^{1/2}/(1 + Pr^{-1/2})$ is the scaling (28) for $v_{m,y,s}$.

E. Validation of the scalings for the Nusselt number

The scaling for Nu_y at the SUS is Eq. (22), which shows that, with the exception of Pr, all other parameters (Ra, s, f_n and y) have effects. This is clearly validated by the numerical results presented in the left column in Fig. 13, as only the time series of Nu_y at different Pr values (DNS runs 3, 9-12), as shown in Fig. 13(d), do not vary at the SUS, while the time series of Nu_y at other parameters differ from each other.

The scaling for $Nu_{y,s}$ at the QSS is Eq. (29), which indicates that all parameters (Ra, Pr, s, f_n, and y) have effects on $Nu_{y,s}$. All these effects are clearly demonstrated by the numerical results presented in the right column in Fig. 13, although the effect of Pr is much small than that of others.

To quantify the scaling (22) for Nu_y, the raw and scaled time series of all 16 DNS runs, each at a specific y value which is randomly selected, are presented in Fig. 14. From Fig. 14(b), it is seen that all scaled time series of Nu_y plotted against $[\sin(2\pi f_n\tau)+s(1-y)]Ra^{1/4}/\tau^{1/2}$ within the SUS are essentially on the same line represented by

$$Nu_y = 0.563\frac{[\sin(2\pi f_n\tau)+s(1-y)]Ra^{1/4}}{\tau^{1/2}}, \tag{46}$$

which confirms and quantified the scaling (22) for Nu_y.

The scaling for $Nu_{y,s}$ at the QSS is Eq. (29). To see if this scaling can be validated by the numerical results, the numerically obtained $Nu_{y,s}$ values for all DNS runs, with each run at the five heights, are plotted in Fig. 15. From Fig. 15(b), it is seen that the scaling (29) for $Nu_{y,s}$, which is $\hat{Nu}_{y,s} = [\sin(2\pi f_n\tau_s)+s(1-y)][\sin(2\pi f_n\tau_s)+s]^{1/4}Ra^{1/4}/(1+Pr^{-1/2})^{1/2}/y^{1/4}$, collapses the numerically obtained $Nu_{y,s}$ approximately onto the following straight line, which is the linear fit obtained with the regression analysis with all data presented in Fig. 15(b),

$$\begin{aligned} N_{y,s} &= 0.514\hat{Nu}_{y,s} + 8.443 \\ &= 0.514\frac{[\sin(2\pi f_n\tau_s)+s(1-y)][\sin(2\pi f_n\tau_s)+s]^{1/4}Ra^{1/4}}{(1+Pr^{-1/2})^{1/2}y^{1/4}} + 8.443, \end{aligned} \tag{47}$$

with the regression constant of $R = 0.9972$. The slope of 0.514 in the above equation represents the quantified empirical proportional constant between $Nu_{y,s}$ and $\hat{Nu}_{y,s}$. The results in the figure show that the deviations of the numerically obtained $Nu_{y,s}$ values away from the above linear fit are much smaller than that of the other parameters.

Accepted to Phys. Fluids 10.1063/5.0191550

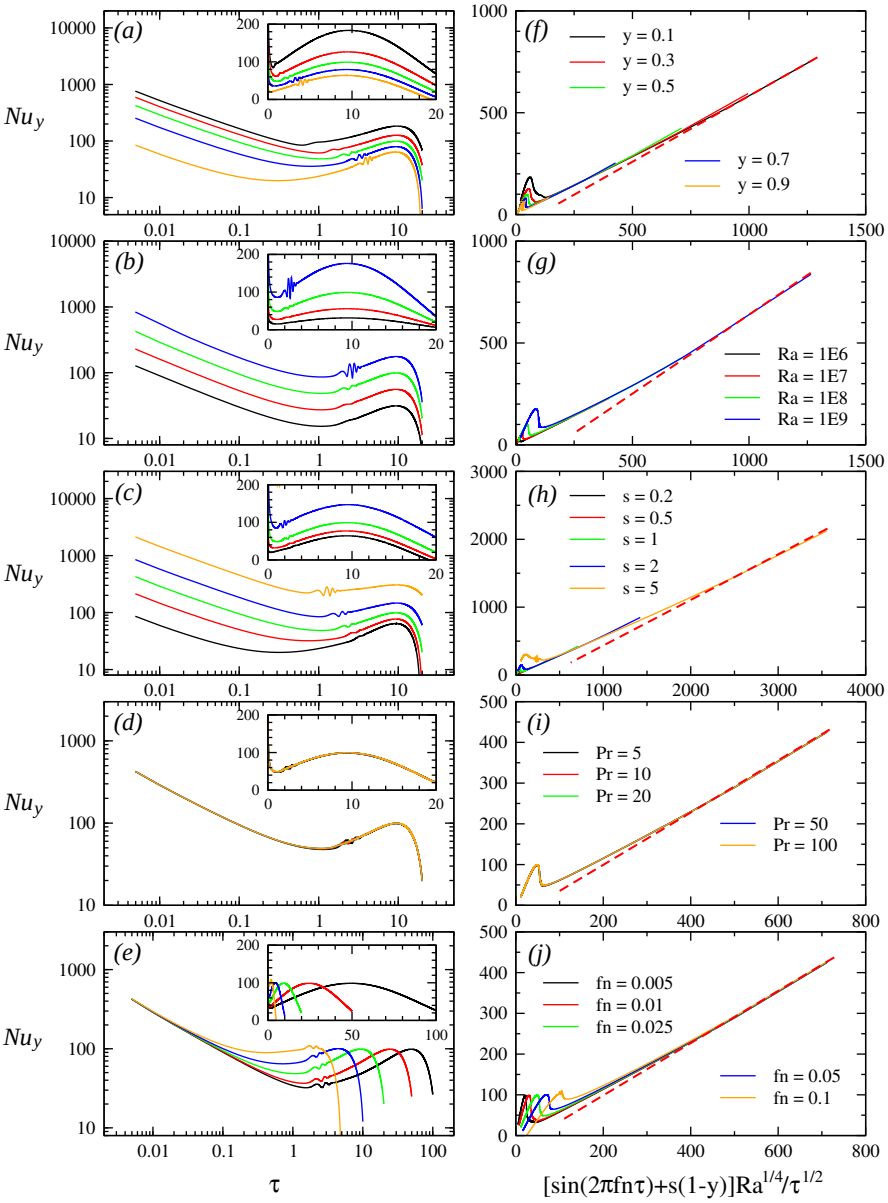

FIG. 13. Time series of Ny_y: raw data (left column) and scaled data (right column): (a) and (f) Run 3 with varying y; (b) and (g) Runs 1-4 with varying Ra at $y = 0.5$; (c) and (h) Runs 3, 5-8 with varying s at $y = 0.5$; (d) and (i) Runs 3, 9-12 with varying Pr at $y = 0.5$; and (e) and (j) Runs 3, 13-16 with varying f_n at $y = 0.5$.

Accepted to Phys. Fluids 10.1063/5.0191550

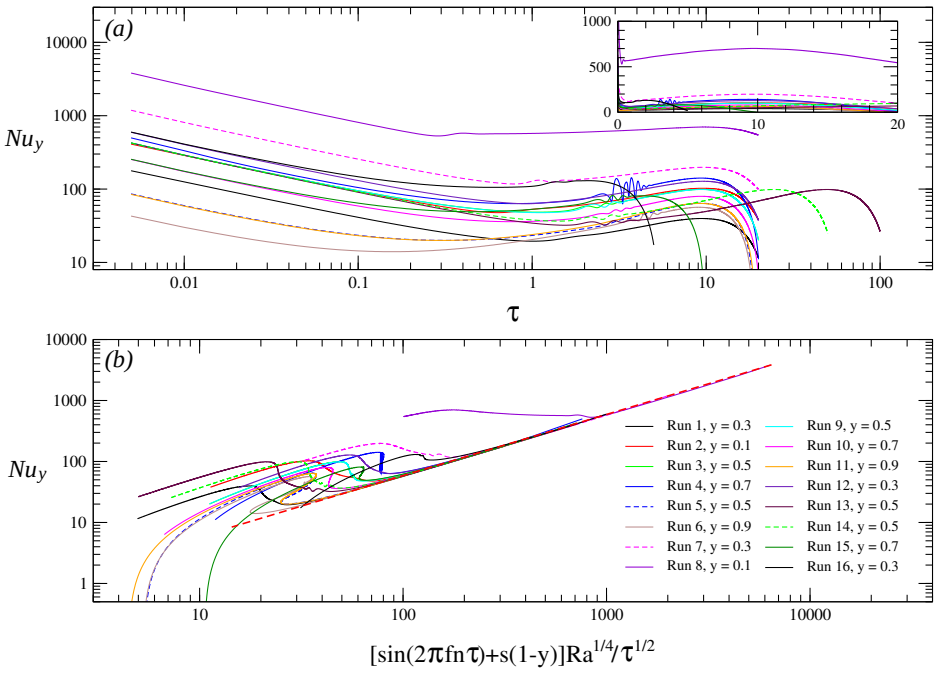

FIG. 14. (*a*) Nu_y plotted against τ (raw data) and (*b*) Nu_y plotted against $[\sin(2\pi f_n\tau) + s(1-y)]Ra^{1/4}/\tau^{1/2}$ (scaled data) for all 16 DNS runs, each at a specific y value. The red dashed line in (*b*) is the slope of Nu_y plotted against $[\sin(2\pi f_n\tau) + s(1-y)]Ra^{1/4}/\tau^{1/2}$, which represents $Nu_y = 0.563[\sin(2\pi f_n\tau) + s(1-y)]Ra^{1/4}/\tau^{1/2}$.

F. Average frequency of fluctuations

As presented and observed above, there are fluctuations in the time series of $\delta_{T,y}$, $\delta_{vi,y}$, $v_{m,y}$ and $\theta_{w,y}$, mainly in the transitional stage. Such fluctuations are expected, as it has been proved that in a linearly-stratified ambient fluid, a flow will experience fluctuations at the Brunt-V*äisälä* N given by[49],

$$N = \left[g\beta\frac{dT_{a,0}(Y)}{dY}\right]^{1/2}. \tag{48}$$

It has been shown that this is true in unsteady NCBL in a linearly-stratified ambient fluid, as we observed in some of our previous studies[21,42].

Accepted to Phys. Fluids 10.1063/5.0191550

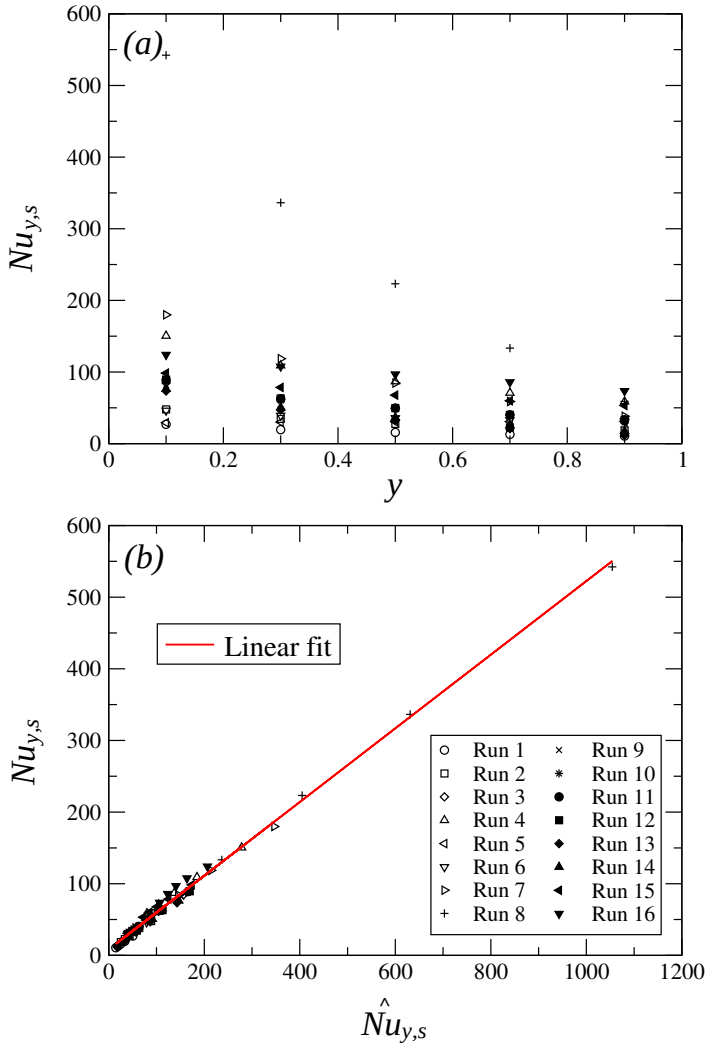

FIG. 15. (a) $Nu_{y,s}$ plotted against y (raw data) and (b) $Nu_{y,s}$ plotted against $\hat{Nu}_{y,s}$ (scaled data) for all 16 DNS runs, each at five y value (y = 0.1, 0.3, 0.5, 0.7, and 0.9). The red line in (b) represents the linear fit between $Nu_{y,s}$ and $\hat{Nu}_{y,s}$, where $\hat{Nu}_{y,s} = [\sin(2\pi f_n \tau_s) + s(1-y)][\sin(2\pi f_n \tau_s) + s]^{1/4} Ra^{1/4}/(1+Pr^{-1/2})^{1/2}/y^{1/4}$ is the scaling (29) for $Nu_{y,s}$.

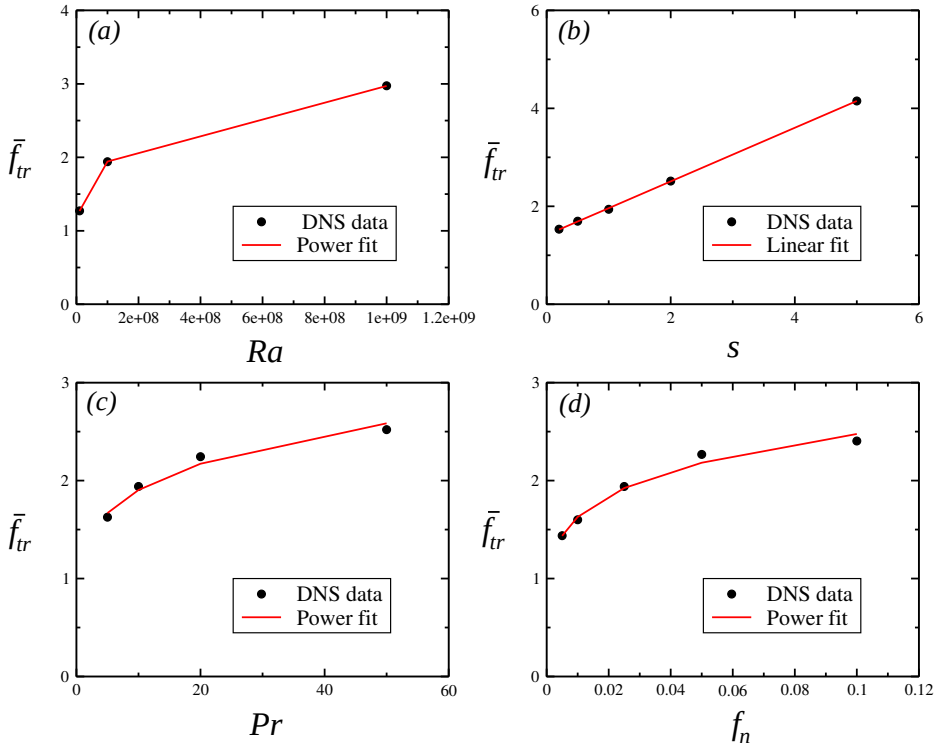

FIG. 16. $\bar{f}_{tr}$ plotted against (a) Ra for the DNS cases 2-4; (b) s for the DNS cases 3, 5-8; (c) Pr for the DNS cases 3, 9-12; and (d) f_n for the DNS cases 3, 13-16, respectively.

In our study on the unsteady NCBL on a vertical isothermal plate in a linearly stratified fluid with $Pr > 1$, it was observed that there are fluctuations in the time series of $\delta_{T,y}$ and $v_{m,y}$, but we did not make an analysis of the feature of the fluctuations[42]. However, in our study on the unsteady NCBL of a linearly-stratified ambient fluid with $Pr < 1$ on an evenly heated semi-infinite vertical plate, we noted very strong fluctuations in the time series of all characteristic parameters of the flow, *i.e.*, $\delta_{T,y}$, $\delta_{vi,y}$, $v_{m,y}$ and $\theta_{w,y}$, which is the dimensionless temperature on the plate at y, in the transitional stage, which is quite long compared to what shown in the present case[21]. We derived, and verified with our numerical simulation

results, that the fluctuations are at the following frequency f_{tr},

$$f_{tr} \sim sPr^{1/2}. \tag{49}$$

However, this scaling for f_{tr} is for the heat flux case applied on the plate which does not vary with time.

For the present case, what applied on the plate is not heat flux, but temperature, which is also not constant but varies with time sinusoidally. In addition, f_n and Ra, which are not present in the constant heat flux case considered in Lin *et al.*,[21], may have effects on f_{tr} as well. To examine the effects of Ra, Pr,s and f_n on f_{tr} for the case considered in the present study, the average value of f_{tr}, $\bar{f}_{tr}$, which is the average of f_{tr} along the plate (*i.e.*, the average of f_{tr} at y = 0.1, 0.3, 0.5, 0.7 and 0.9), is obtained for each DNS runs with the numerical results for $\delta_{T,y}$, with the results presented in Fig. 16. It is expected that $\bar{f}_{tr}$ obtained from the $\delta_{T,y}$ results is the same for $\delta_{vi,y}$, $v_{m,y}$ and Nu_y as well. It should be pointed out that for some DNS cases, either the magnitudes of the fluctuations are negligible or no fluctuations at some heights at all, as shown in the time series of $\delta_{T,y}$, $\delta_{vi,y}$, $v_{m,y}$ and Nu_y in the relevant figures presented above, which results in noticeable inaccuracy of the obtained values of $\bar{f}_{tr}$.

Figure 16 demonstrates that all four control parameters (Ra, Pr, s, and f_n) have effects on $\bar{f}_{tr}$ for the time-varying temperature case considered in the present study. It is found that $\bar{f}_{tr}$ increases with Ra, as shown in Fig. 16(a), which can be correlated approximately by a power fit; increases linearly with s almost perfectly, as shown in Fig. 16(b), which is in agreement with the scaling (49) even this scaling is for the constant heat flux case; increases with Pr, as shown in Fig. 16(c), which is found to be correlated reasonably well with $Pr^{1/2}$ (not shown in the figure), which is also in good agreement with the scaling (49); and increases with f_n, as shown in Fig. 16(d), which can be correlated well by a power-fit too.

V. CONCLUSIONS

A set of scalings for the key parameters characterizing the behavior of unsteady NCBL flow of a linearly-stratified $Pr > 1$ fluid on a semi-infinite vertical solid surface heated with a time-varying sinusoidal temperature are developed with a scaling analysis. These parameters

include the maximum vertical velocity within the boundary layer, thermal boundary-layer thickness, inner viscous boundary-layer thickness, Nusselt number, and the relevant time scale. The scalings are represented in terms Ra, Pr, s and f_n, which are the major controlling parameters of the flow.

It is found that the unsteady NCBL experiences three distinct development stages; the start-up stage, the transitional stage, and the quasi-steady stage, and the scalings for each parameter are different at different stages. The obtained scalings are validated and quantified with 16 DNS runs over $10^6 \leq Ra \leq 10^9$, $0.2 \leq s \leq 5$, $5 \leq Pr \leq 100$, and $0.005 \leq f_n \leq 0.1$. It is found that the numerical results are in general in good agreement with the scalings, verifying the effects of these controlling parameters.

At the transitional stage, due to the stratification of the ambient fluid, there are fluctuations in the time series of the behavior characteristic parameters at the Brunt-V*äisälä* frequency. The numerical results show that the previously obtained scaling for the fluctuation frequency for the unsteady NCBL on a vertical isothermal plate in a linearly stratified fluid with $Pr > 1$ with the constant applied heat flux, in terms of s and Pr only, is basically applicable for the case considered in the present study as well, but the frequency is also influenced additionally by Ra and f_n due to the time-varying nature of the applied temperature.

CONFLICT OF INTERESTS

The authors declare that there are no conflict of interests.

DATA AVAILABILITY STATEMENT

The data that supports the findings of this study are available from the corresponding author upon reasonable request.

ORCID

Wenxian Lin: http://orcid.org/0000-0001-5264-2097
S. W. Armfield: http://orcid.org/0000-0002-8032-0017
Mehdi Khatamifar: http://orcid.org/0000-0001-6273-7655

Accepted to Phys. Fluids 10.1063/5.0191550

REFERENCES

[1]Bhowmick S, Xu F, Zhang X, Saha SC. Natural convection and heat transfer in a valley shaped cavity filled with initially stratified water. Int J Heat Mass Transfer. 2018;128:59-64.

[2]Liu Y. Scaling of convective boundary layer flow induced by linear thermal forcing at $Pr < 1$ and $Pr > 1$. Phys Rev E. 2019;100:043112.

[3]Zhao Y, Zhao P, Liu Y, Xu Y, Torres JF. On the selection of perturbations for thermal boundary layer control. Phys Fluids. 2019;31:104102.

[4]Lyer KP, Scheel JD, Schumacher J, Sreenivasana K. Classical 1/3 scaling of convection holds up to $Ra = 10^{15}$. PANS. 2020;117(14):7594-7598.

[5]Liu Y. Dynamics and scale analysis of the transient convective flow induced by cooling a $Pr < 1$ fluid with linear thermal forcing. Int J Heat Mass Transfer. 2020;154:119767.

[6]Ke J, Williamson N, Armfield SW, Norris SE, Komiya A. Law of the wall for a temporally evolving vertical natural convection boundary layer. J Fluid Mech, 2020;902:A31.

[7]Ke J, Williamson N, Armfield SW, Komiya A, Norris SE. High Grashof number turbulent natural convection on an infinite vertical wall. J Fluid Mech. 2021;929:A15.

[8]Fan Y, Zhao Y, Torres JF, Xu F, Lei C, Li Y, Carmeliet J. Natural convection over vertical and horizontal heated flat surfaces: A review of recent progress focusing on underpinnings and implications for heat transfer and environmental applications. Phys Fluids. 2021;33:101301.

[9]Priam SS, Ikram MM, Saha S, Saha SC. Conjugate natural convection in a vertically divided square enclosure by a corrugated solid partition into air and water regions. Therm Sci Eng Prog. 2021;25:101036.

[10]Nie B, Shao Y, Xu F. An experimental study of natural convection on a vertical surface with neighboring isothermal and isoflux heating. Eur Phys J E 2021;44:104.

[11]Lin W, Armfield SW, Khatamifar M, Scaling laws for natural convection boundary layer of a $Pr > 1$ fluid on a vertical solid surface subject to a sinusoidal heating flux in a linearly stratified ambient. Heat Transf. 2022;51:2956-2976.

[12]Nie B, Xu F. Effect of curvature on transient natural convection in a vertical circular pipe. J Fluid Mech. 2022;937:A29.

[13]Duffie JA, Beckman WA. *Solar Engineering of Thermal Processes* (4th Edn). New York:

John Wiley & Sons; 2013.

[14]Faghri A, Zhang Y, Howell J. *Advanced Heat and Mass Transfer*. Columbia, MO: Global Digital Press; 2010.

[15]Sergei K, Shen C, Jiang Y. A review of the current work potential of a trombe wall. Renew Sustain Energy Rev. 2020;130:109947.

[16]Fudholi A, Sopian K. A review of solar air flat plate collector for drying application. Renew Sustain Energy Rev. 2019;102:333-345.

[17]Hu J, Liu K, Guo M, Zhang G, Chu Z, Wang M. Performance improvement of baffle-type solar air collector based on first chamber narrowing. Renew Energy. 2019;135:701-710.

[18]Khanal R, Lei C. A scaling investigation of the laminar convective flow in a solar chimney for natural ventilation. Int J Heat Fluid Flow. 2014;45:98-108.

[19]Monghasemi N, Vadiee A. A review of solar chimney integrated systems for space heating and cooling application. Renew Sustain Energy Rev. 2018;81:2714-2730.

[20]Ren X, Wang L, Liu R, Wang L, Zhao F. Thermal stack airflows inside the solar chimney with discrete heat sources: Reversal flow regime defined by chimney inclination and thermal Rayleigh number. Renew Energy. 2021;163:342-356.

[21]Lin W, Armfield SW, Patterson JC. Unsteady natural convection boundary-layer flow of a linearly-stratified fluid with $Pr \lesssim 1$ on an evenly heated semi-infinite vertical plate. Int J Heat Mass Transfer. 2008;51:327-343.

[22]Lin W, Armfield SW, Patterson JC, Lei C. Prandtl number scaling of unsteady natural convection boundary layers for Pr¿1 fluids under isothermal heating. Phys Rev E. 2009;79:066313.

[23]Bednarz T, Lin, W, Patterson, JC, Lei, C, Armfield, SW. Scaling for unsteady thermomagnetic convection boundary layer of paramagnetic fluids of $Pr > 1$ in micro-gravity conditions. Int J Heat Fluid Flow. 2009;30(6):1157-1170.

[24]Lin W, Armfield SW. Unified Prandtl number scaling for start-up and fully developed natural-convection boundary layers for both $Pr \gtrsim 1$ and $Pr \lesssim 1$ fluids with isothermal heating. Phys Rev E. 2012;86:066312.

[25]Saha S, Brown R, Gu Y. Prandtl number scaling of the unsteady natural convection boundary layer adjacent to a vertical flat plate for $Pr > 1$ subject to ramp surface heat flux. Int J Heat Mass Transfer. 2012;55:7046-7055.

[26]Lin W, Armfield SW. Scalings for unsteady natural convection boundary layers on an

evenly heated plate with time-dependent heat flux. Phys Rev E. 2013;88:063013.

[27]Lin W, Armfield SW. Scalings for unsteady natural convection boundary layers on a vertical plate at time-dependent temperature. Int J Thermal Sci. 2017;111:78-99.

[28]Hussam WK, Khanafer K, Salema HG, Sheard GI. Natural convection heat transfer utilizing nanofluid in a cavity with a periodic side-wall temperature in the presence of a magnetic field. Int Communi Heat Mass Transfer. 2019;104:127-135.

[29]Mao Y, Lei C, Patterson, JC. Unsteady natural convection in a triangular enclosure induced by absorption of radiation – a revisit by improved scaling analysis. J Fluid Mech. 2009;622:75-102.

[30]Liu Y, Bian Y, Zhao Y, Zhang S, Suo Q. Scaling laws for the transient convective flow in a differentially and linearly heated rectangular cavity at Pr ¿ 1. Phys Fluids. 2019;31:043601.

[31]Liu Y, Ren S. Scale law analysis of the curved boundary layer evolving around a horizontal cylinder at Pr ¿ 1. Phys Fluids. 2021;33:073614.

[32]Liu Y, Huang H. Effect of three modes of linear thermal forcing on convective flow and heat transfer in rectangular cavities. Int J Heat Mass Transfer. 2020;147:118951.

[33]Nie B, Xu F. Scales of natural convection on a convectively heated vertical wall. Phys Fluids. 2019;31:024107.

[34]Khatamifar M, Lin W, Dong L. Transient conjugate natural convection heat transfer in a differentially-heated square cavity with a partition of finite thickness and thermal conductivity. Case Studies Thermal Eng. 2021;25:100952.

[35]Bala NR, Bala SK, Saha LK, Hossain MA. Influence of undulating wall heat and mass flux on MHD natural convection boundary layer flow from a vertical wall. Heat Transfer. 2021;50:818–848

[36]Liu Y, Ren S. Improved scaling analysis of the transient buoyancy-driven flow induced by a linear temperature gradient. Int J Heat Mass Transfer. 2020;162:120386.

[37]Zhou L, Armfield SW, Williamson N, Kirkpatrick MP, Lin W. Natural convection in a cavity with time-varying thermal forcing on a sidewall. Int J Heat Mass Transfer. 2020;150:119234.

[38]Zhou L, Armfield SW, Williamson N, Kirkpatrick MP, Lin W. Natural convection in a cavity with time-dependent flux boundary. Int J Heat Fluid Flow. 2021;92:108887.

[39]Loenko DS, Shenoy A, Sheremet MA. Effect of time-dependent wall temperature on natural convection of a non-Newtonian fluid in an enclosure. Int J Thermal Sci. 2021;166:106973.

[40]Wu F, Wang G. Numerical simulation of natural convection in an inclined porous cavity under time-periodic boundary conditions with a partially active thermal side wall. RPC Adv. 2017;7:17519-17530.

[41]He W, Qin G, Wang Y, Bao Z. A segregated spectral element method for thermomagnetic convection of paramagnetic fluid in rectangular enclosures with sinusoidal temperature distribution on one side wall. Numer Heat Transfer A: Applications. 2019;76(2):51–72.

[42]Lin W, Armfield SW, Morgan PL. Unsteady natural convection boundary-layer flow along a vertical isothermal plate in a linearly stratified fluid with $Pr > 1$. Int J Heat Mass Transfer. 2002;45:451-459.

[43]Lin W, Armfield SW. Unsteady natural convection on an evenly heated vertical plate for Prandtl number $Pr < 1$. Phys Rev E. 2005;72:066309.

[44]Armfield SW, Patterson JC, Lin W. Scaling investigation of the natural convection boundary layers on an even heated plate. Int J Heat Mass Transf. 2007;50:1592-1602.

[45]Lin W, Armfield SW. Natural convection boundary-layer flow on an evenly heated vertical plate with time-varying heating flux in a stratified Pr ¡ 1 fluid. Numer Heat Transfer. A: Applications. 2019;76(6):393–419.

[46]Lin W, Armfield SW. Prandtl number scalings for unsteady natural convection boundary-layer flow on an evenly heated vertical plate in a homogeneous Pr ¿ 1 fluid. Numer Heat Transfer A: Applications. 2020;77(6):619–631.

[47]Lin W, Armfield SW, Khatamifar M. Scalings for unsteady natural convection boundary layer under time-varying heating flux in a small Prandtl number fluid. Case Studies Thermal Eng. 2021;27:101351.

[48]Lin W, Armfield SW, Patterson JC. Cooling of a $Pr < 1$ fluid in a rectangular container. J Fluid Mech. 2007;574:85–108.

[49]Turner JS. *Buoyancy Effects in Fluids*. Cambridge: Cambridge University Press; 1973.